

A climatological study of evapotranspiration and moisture stress across the continental United States based on thermal remote sensing:

1. Model formulation

Martha C. Anderson,¹ John M. Norman,² John R. Mecikalski,³ Jason A. Otkin,⁴ and William P. Kustas¹

Received 12 May 2006; revised 26 October 2006; accepted 30 January 2007; published 24 May 2007.

[1] Due to the influence of evaporation on land-surface temperature, thermal remote sensing data provide valuable information regarding the surface moisture status. The Atmosphere-Land Exchange Inverse (ALEXI) model uses the morning surface temperature rise, as measured from a geostationary satellite platform, to deduce surface energy and water fluxes at 5–10 km resolution over the continental United States. Recent improvements to the ALEXI model are described. Like most thermal remote sensing models, ALEXI is constrained to work under clear-sky conditions when the surface is visible to the satellite sensor, often leaving large gaps in the model output record. An algorithm for estimating fluxes during cloudy intervals is presented, defining a moisture stress function relating the fraction of potential evapotranspiration obtained from the model on clear days to estimates of the available water fraction in the soil surface layer and root zone. On cloudy days, this stress function is inverted to predict the soil and canopy fluxes. The method is evaluated using flux measurements representative at the watershed scale acquired in central Iowa with a dense flux tower network during the Soil Moisture Experiment of 2002 (SMEX02). The gap-filling algorithm reproduces observed fluxes with reasonable accuracy, yielding ~20% errors in ET at the hourly timescale, and 15% errors at daily timesteps. In addition, modeled soil moisture shows reasonable response to major precipitation events. This algorithm is generic enough that it can easily be applied to other thermal energy balance models. With gap-filling, the ALEXI model can estimate hourly surface fluxes at every grid cell in the U.S. modeling domain in near real-time. A companion paper presents a climatological evaluation of ALEXI-derived evapotranspiration and moisture stress fields for the years 2002–2004.

Citation: Anderson, M. C., J. M. Norman, J. R. Mecikalski, J. A. Otkin, and W. P. Kustas (2007), A climatological study of evapotranspiration and moisture stress across the continental United States based on thermal remote sensing: 1. Model formulation, *J. Geophys. Res.*, 112, D10117, doi:10.1029/2006JD007506.

1. Introduction

[2] Given current trends in population growth and climate change, it will become increasingly critical to be able to accurately monitor the earth's water resources at regional, continental, and global scales. One component of the land surface water budget that can be readily monitored by satellite is water loss to the atmosphere, or evapotranspiration (ET). Robust, operational methodologies for mapping ET, soil moisture, and moisture stress over large areas

using remote sensing will have widespread utility in a variety of resource management and forecasting applications. Evapotranspiration is a critical variable in hydrologic modeling: for forecasting river stage and flood potential, and for constraining recharge in groundwater simulations. ET and other surface fluxes provide important boundary conditions for numerical weather prediction and general circulation models. Routine spaceborne soil moisture and moisture stress mapping will also benefit efforts in drought detection, yield forecasting, fire prediction, and agricultural and military trafficability assessment.

[3] Prognostic assessments of evapotranspiration using water budget models such as the Variable Infiltration Capacity [VIC; *Liang et al.*, 1994; *Wood et al.*, 1992] model and the Soil and Water Assessment Tool [SWAT; *Arnold et al.*, 1998] require input fields of spatially distributed precipitation, derived through surface gauge networks, radar, satellite imagery, and/or modeling. In these models, ET is regulated by the moisture content in the soil profile,

¹USDA-ARS Hydrology and Remote Sensing Laboratory, Beltsville, Maryland, USA.

²Department of Soil Science, University of Wisconsin, Madison, Wisconsin, USA.

³National Space Science and Technology Center, University of Alabama, Huntsville, Alabama, USA.

⁴Cooperative Institute for Meteorological Satellite Studies, University of Wisconsin, Madison, Wisconsin, USA.

which is updated each timestep based on predicted infiltration and depletion rates. These rates depend strongly on the accuracy of the input fields of precipitation and soil hydraulic properties, quantities that are difficult to specify at regional or continental scales, and on the accuracy of the soil model itself [Beljaars *et al.*, 1996]. Biases in these fields result in cumulative errors in soil moisture pools and associated fluxes, which can become large in the long-term if there are no mechanisms for periodic correction [Betts *et al.*, 1997; Schaake *et al.*, 2004].

[4] In contrast, diagnostic satellite assessments can accomplish a complete update of the current surface moisture state whenever the remote sensing data are available. In general, these models do not require precipitation as an input, nor do they need information about subsurface soil texture: instantaneous ET rates are linked to observables like land-surface temperature and vegetation cover fraction. Examples of this type of modeling approach include the Surface Energy Balance System [SEBS; Su, 2002], the Surface Energy Balance Algorithm for Land [SEBAL; Bastiaanssen *et al.*, 1998], the temperature/NDVI (Normalized Difference Vegetation Index) triangle method [Gillies *et al.*, 1997], and the Two-Source Energy Balance model [TSEB; Norman *et al.*, 1995]. The disadvantage to diagnostic modeling is that the output record often suffers large spatial and temporal gaps due to cloud cover and infrequent image availability as governed by the satellite overpass schedule.

[5] In this and in a companion paper [Anderson *et al.*, 2007b, hereinafter referred to as A2], we investigate the utility of a thermal infrared (TIR) remote sensing approach to monitoring ET at continental scales that incorporates methods for addressing the spatiotemporal limitations of diagnostic modeling. The Atmosphere-Land Exchange Inverse (ALEXI) model [Anderson *et al.*, 1997] is unique among existing thermal ET models in that:

[6] (a) ALEXI is based on a two-source land-surface representation (the TSEB), which treats the land surface as a composite of soil and vegetation elements with different temperatures, fluxes, and atmospheric coupling. This results in a single model formulation that can be applied to a wide range of canopy and moisture stress conditions, including partially vegetated surfaces.

[7] (b) ALEXI inherently uses the high-temporal resolution (~hourly) information provided by geostationary satellites to reduce sensitivity to sensor bias and to provide time-continuous flux predictions over continental scales.

[8] Mecikalski *et al.* [1999] recorded an initial attempt at a regional-scale application of ALEXI over the central U.S. using observations from the Geostationary Operational Environmental Satellite (GOES). The input data sources and modeling techniques have been subsequently improved, and now include a means for deducing moisture stress and available soil water from modeled ET rates. In addition, techniques have been developed for predicting fluxes on cloudy days when thermal satellite imagery is not available, and for extrapolating instantaneous fluxes estimated at discrete imaging times to full hourly coverage at each grid cell in the modeling domain. Vegetation cover fraction is derived from the Moderate Resolution Imaging Spectroradiometer (MODIS) leaf area index product (MOD15A).

[9] In this paper we describe the enhancements made to the model and demonstrate the gap-filling technique in comparison with large-scale flux measurements from the Soil Moisture-Atmospheric Coupling Experiment of 2002 [SMACEX; Kustas *et al.*, 2005]. In A2, a 3-year climatological analysis of continental-scale evaporative fluxes and moisture stress at 10-km spatial resolution over the U.S. will be presented. Ultimately, a coupling of prognostic and diagnostic modeling systems may provide the optimal means for performing time-continuous hydrologic monitoring over large spatial scales.

2. Model Description

2.1. The ALEXI Model

2.1.1. Interpretation of the Thermal Land-Surface Signature

[10] Surface energy balance models estimate ET by partitioning the energy available at the land surface ($RN - G$, where RN is net radiation and G is the soil heat conduction flux, in W m^{-2}) into turbulent fluxes of sensible and latent heating (H and λE , respectively, W m^{-2}):

$$RN - G = H + \lambda E \quad (1)$$

where λ is the latent heat of vaporization (J kg^{-1}) and E is evapotranspiration ($\text{kg s}^{-1} \text{ m}^{-2}$ or mm s^{-1}). Surface temperature is a valuable metric for constraining λE because varying soil moisture conditions yield a distinctive thermal signature: moisture deficiencies in the root zone lead to vegetation stress and elevated canopy temperatures, while depletion of water from the soil surface layer causes the soil component of the scene to heat up rapidly.

[11] The land-surface representation in ALEXI model is based on the series version of the two-source energy balance model of Norman *et al.* [1995; see also Kustas and Norman, 1999, 2000]. The TSEB partitions the composite surface radiometric temperature, T_{RAD} , into characteristic soil and canopy temperatures, T_s and T_c , based on the local vegetation cover fraction apparent at the thermal sensor view angle, $f(\theta)$:

$$T_{\text{RAD}}(\theta) \approx f(\theta)T_c + [1 - f(\theta)]T_s \quad (2)$$

(Figure 1), where equation 2 is a linear approximation to an aggregation of surface radiance values. With this information, the TSEB evaluates the soil (subscript 's') and the canopy ('c') energy budgets separately, computing system and component fluxes of net radiation ($RN = RN_c + RN_s$), sensible and latent heat ($H = H_c + H_s$ and $\lambda E = \lambda E_c + \lambda E_s$), and soil heat conduction (G). Because angular effects are incorporated into the decomposition of T_{RAD} , the TSEB can accommodate thermal data acquired at off-nadir viewing angles and can therefore be applied to geostationary satellite images. An overview of the TSEB equation set is given in Appendix A.

[12] The TSEB has a built-in mechanism for detecting thermal signatures of stress in the soil and canopy. A modified Priestley-Taylor (PT) relationship [Priestley and Taylor, 1972], applied to the divergence of net radiation within the canopy (RN_c), provides an initial estimate of canopy transpiration [λE_c ; Tanner and Jury, 1976], while

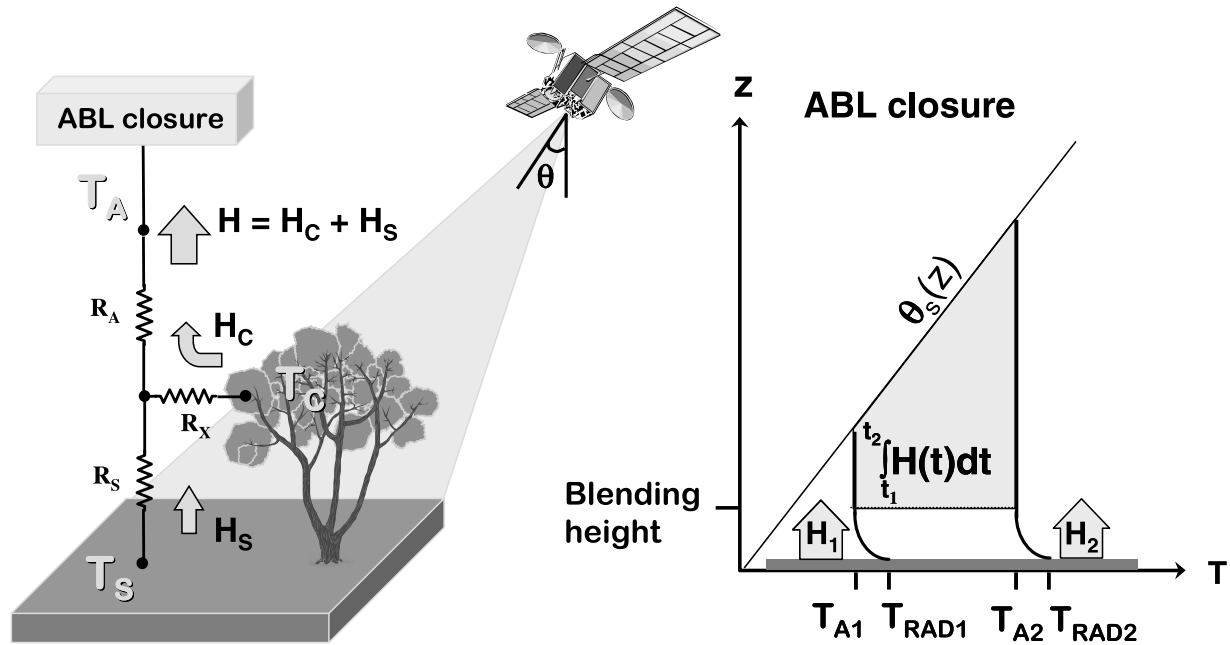


Figure 1. Schematic diagram representing the two-source land-surface scheme (left) and the time-integrated ABL closure component (right) of the ALEXI model.

the soil evaporation rate (λE_S) is computed as a residual to the system energy budget. If the vegetation is stressed and transpiring at significantly less than the potential rate, the PT equation will overestimate λE_C and the residual λE_S will become negative. Condensation onto the soil is unlikely midday on clear days, and therefore $\lambda E_S < 0$ is considered a signature of system stress. Under such circumstances, the PT coefficient is throttled back until $\lambda E_S \sim 0$ (expected under dry conditions). Both λE_C and λE_S will then be some fraction of the potential ET rates associated with the canopy and soil components of the scene; these ratios are integral to the soil moisture estimation scheme described below.

2.1.2. Regional-Scale Boundary Conditions and Execution

[13] For regional-scale applications of the TSEB model, meteorological boundary conditions in air temperature, T_A in Figure 1, must be specified at the spatial resolution of the thermal data (typically ≤ 10 km). Due to localized feedback between the land and atmosphere, this input field cannot be interpolated with adequate accuracy from standard synoptic measurements, with typical spacing in the U.S. of 100 km. To overcome this limitation, the TSEB has been coupled with an atmospheric boundary layer model, thereby simulating land-atmosphere feedback and its effect on local air temperature internally. In the ALEXI model, the TSEB is applied at two times during the morning ABL growth phase (approximately $t_1 = 1.5$ and $t_2 = 5.5$ h after local sunrise), using radiometric temperature data obtained from a geostationary platform like GOES or Meteosat at spatial resolutions of 5–10 km. Energy closure over this interval is provided by a simple slab model of ABL development [McNaughton and Spriggs, 1986], which relates the rise in air temperature in the mixed layer to the time-integrated influx of sensible heat from the land surface (Figure 1). As a result of this configuration, ALEXI uses only time-differential temperature signals, thereby minimizing flux

errors due to absolute sensor calibration and atmospheric and spatial effects [Kustas *et al.*, 2001]. The primary radiometric signal is the morning surface temperature rise, while the ABL model component uses only the general slope (lapse rate) of the atmospheric temperature profile [Anderson *et al.*, 1997; see also Appendix A], which is more reliably analyzed from synoptic radiosonde data than is the absolute temperature reference.

[14] At each GOES observation time, the TSEB simultaneously balances energy budgets associated with the canopy, the soil and the composite land-surface system. Input data required to execute ALEXI are listed in Table 1 and operational sources are discussed below. Primary outputs from ALEXI are instantaneous values of T_A , G , RN , RN_C , RN_S , λE , λE_C , λE_S , H , H_C , and H_S at times t_1 and t_2 . In addition, the source temperatures T_C and T_S are evaluated at each GOES observation time and have intrinsic value for modeling canopy photosynthesis and soil respiration [Anderson *et al.*, 2000].

2.1.3. Validation

[15] To validate the 5–10 km resolution output fields generated by ALEXI, the coarse-scale flux estimates can be spatially disaggregated to micrometeorological scales resolving the flux sensor footprint (typically of dimension ~ 100 m) using a technique referred to as DisALEXI [Norman *et al.*, 2003]. Anderson *et al.* [2007a] review ALEXI/DisALEXI validation experiments conducted in rangeland and agricultural landscapes in Oklahoma [Anderson *et al.*, 2004b; Norman *et al.*, 2003] and Iowa [Anderson *et al.*, 2005]. Typical root-mean square-deviations (RMSDs) in comparison with tower flux measurements of H and λE are 35–40 Wm^{-2} (15%) at the 30–120 m disaggregation scale. Comparisons of disaggregated fluxes have also been made with respect to transect measurements made with flux aircraft, yielding RMSD values of

Table 1. Primary ALEXI Input Data Sources

Data	Purpose	Source	Product Resolution
Clear sky:			
$T_{\text{RAD1}}, T_{\text{RAD2}}$	Surface temperature change	GOES	5–10 km
LAI	Assign $f(\theta)$, h_c , d , z_0 , ε	MODIS	1 km
Landcover type	Assign h_c , d , z_0 , α , s	UMD global	1 km
Wind	Aerodynamic resistances	ASOS/AWOS	40 km ^a
Lapse rate profile	ABL growth model	Radiosonde	40 km ^a
$\theta_s(z)$, $q_s(z)$	Atmospheric corrections	Radiosonde	40 km ^a
Cloud amount	Cloud mask	GOES	10 km
S_{di} , L_{di}	Hourly net radiation	GOES	20 km
Cloudy sky:			
Soil texture (0–5 cm, 5–200 cm)	Assign AWC	STATSGO	1 km

^aSynoptic data (~100-km spacing) have been analyzed to a 40-km resolution grid within the analysis component of the Cooperative Institute for Meteorological Satellite Studies (CIMSS) mesoscale model [Diak *et al.*, 2003].

35 Wm⁻² for H and λE and accurate reconstruction of observed spatial variability [Kustas *et al.*, 2006].

2.2. Available Water Model

[16] To simulate the effects of soil moisture depletion on evapotranspiration, many prognostic land-surface models use a simple soil moisture stress function relating the model-predicted available water fraction (f_{AW}) to a factor (f_{PET}) used to decrement actual ET (E ; mm s⁻¹) from the potential rate expected under unstressed conditions (PET ; mm s⁻¹):

$$f_{\text{PET}} = \frac{E}{PET}. \quad (3)$$

[17] The available water fraction is defined as the ratio of actual plant-available water (AW) divided by the available water capacity of the soil (AWC):

$$f_{\text{AW}} = \frac{AW}{AWC} = \frac{(\theta - \theta_{\text{wp}}) \times d}{(\theta_{\text{fc}} - \theta_{\text{wp}}) \times d} \quad (4)$$

where d (mm) is the thickness of the soil layer supplying water to the transpiring vegetation, and θ_{wp} and θ_{fc} (m³ m⁻³) are the volumetric soil water contents at the wilting point and field capacity, respectively, and θ is the current moisture content. The stress function, mapping values of f_{AW} to f_{PET} (i.e., $f_{\text{PET}} = \text{fn}[f_{\text{AW}}]$), can be either derived from physical principles, for example relating to soil and plant water potentials [e.g., Campbell and Norman, 1998], or it can be modeled empirically using surface flux and soil moisture observations [e.g., Stewart and Verma, 1992].

[18] In diagnostic models, ET is diagnosed directly from the remote sensing data and therefore the stress function can be inverted ($f_{\text{AW}} = \text{fn}^{-1}[f_{\text{PET}}]$) to infer soil moisture conditions at the time of the image acquisition. The two-source model further partitions ET into soil and canopy components, allowing us to probe dimensionless moisture conditions in the soil surface layer (f_{AWsfc}) and root-zone (f_{AWrz}), respectively, given model estimates of the component PET fractions:

$$f_{\text{PETc}} = \frac{E_c}{PET_c} \quad f_{\text{PETs}} = \frac{E_s}{PET_s} \quad (5)$$

Segregation of these two moisture pools is possible with the TSEB model because moisture content in the plant root-zone regulates transpiration rates, while soil evaporation is driven by moisture within the top few centimeters of the soil profile. The depletion rates associated with these two pools have very different time constants [weeks vs. days, respectively; Kim and Verma, 1990; Brutsaert and Chen, 1995; Porté-Agel *et al.*, 2000]. Once the surface layer has dried, its hydraulic connectivity with the sub-surface is significantly reduced and the two moisture pools become effectively decoupled [Capehart and Carlson, 1997; Carlson *et al.*, 1995].

[19] A wide range of stress functional forms can be found in the literature [Abramopoulos *et al.*, 1988; Brutsaert, 1984], including linear functions [e.g., Mahfouf and Noilhan, 1991], piecewise linear or threshold models [e.g., Mahrt and Pan, 1984], and non-linear forms [e.g., Campbell and Norman, 1998] with varying degrees of complexity and dependence on soil textural properties and vegetation type. Appropriate functions may also depend on the size of the model pixel and sub-pixel heterogeneity in soil conditions [Chen *et al.*, 1996]. For large-scale applications, linear functions are often preferred because the sensitivity to soil moisture is constant, and less detailed information about soil properties is required [Betts *et al.*, 1997; Song *et al.*, 2000].

[20] A qualitative summary of the existing observations of canopy response to moisture stress suggests that $f_{\text{PET}} \sim 1$ as f_{AW} falls from 1 to ~0.5, and then f_{PET} decreases approximately linearly toward 0 for smaller values of f_{AW} . ALEXI uses a normalized logistic function that captures these characteristics without discontinuity:

$$f_{\text{PET}} = \text{fn}[f_{\text{AW}}] = \frac{\ln(W)}{\ln(W_f)} \quad (6a)$$

where

$$W = \frac{W_0 W_f}{W_0 + (W_f - W_0) \exp(-\mu f_{\text{AW}})} \quad (6b)$$

is a logistic growth equation commonly used in agricultural modeling [e.g. France and Thornley, 1984] and $W_0 = 1$, $W_f = 800$, and $\mu = 12$ (see Figure 2). The μ parameter controls the position and sharpness of the cutoff. The functional in equation 6 qualitatively reproduces the expected behavior while remaining independent of soil

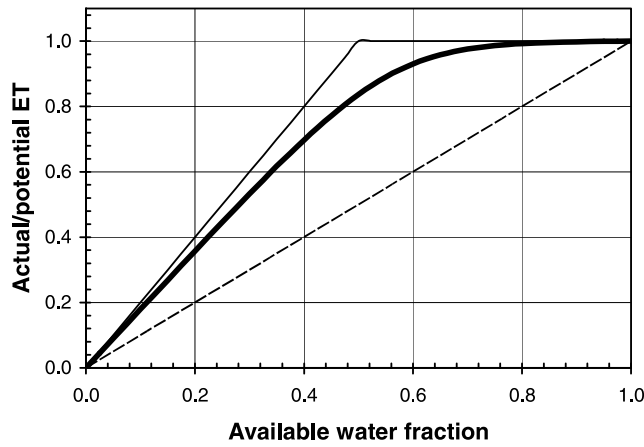


Figure 2. Soil moisture stress function (equation 6) used in the gap-filling algorithm, relating f_{PET} to AWF (thick solid line). Also, shown are simple functions used in other modeling frameworks, including linear (dashed) and piecewise linear (thin solid) relationships.

texture. While stress functions like equation 6 more generally refer to vegetation response to soil moisture, the overall characteristics of the function mimic those of the two-stage soil drying process, with a potential evaporation stage 1 phase, and a second stage where the evaporation rate decreases non-linearly [Ritchie, 1972]. For the sake of simplicity, the same functional is applied here to both canopy transpiration and soil evaporation.

[21] In this study, estimates of potential soil and canopy ET have been based on the Priestley-Taylor approximation [Priestley and Taylor, 1972; see Appendix B]. While this approximation may underestimate latent heat flux when the vapor pressure deficit of the atmosphere is large [Kustas and Norman, 1999], it is used to maintain consistency with the method used to predict canopy transpiration in the TSEB and because it requires minimal parameterization. In future applications, the Priestley-Taylor coefficient could be varied geographically as a function of vapor pressure deficit or canopy conductance.

2.3. Gap-Filling Techniques

[22] ALEXI requires clear-sky conditions during the time interval t_1 to t_2 to obtain the required surface temperature data and to satisfy model assumptions of linear sensible heat rise during the morning boundary layer growth phase (equation A16). As an example, the map of solar radiation for 30 April 2003 in Figure 3a reveals a thick band of clouds covering the northern states of the U.S. at time t_2 , while Figure 3b shows the distribution of pixels passing the t_1 – t_2 cloud screening and other input tests, where latent heat could be directly computed on this day. For 2002–2004, ALEXI provided on average 30% daily coverage over the continental US. To facilitate climatological investigations of land-surface fluxes, simple techniques for filling extant gaps in ALEXI coverage have been investigated.

[23] The filling of fluxes on cloudy days is accomplished by maintaining running pools of available water for the root zone (5–200 cm) and soil surface layer (0–5 cm) at each pixel: $AW_{rz} = f_{AW_{rz}} \times AWC_{rz}$ and $AW_{sfc} = f_{AW_{sfc}} \times AWC_{sfc}$, respectively. These pools are updated via inversion of

equation 6 on days when the pixel is clear, using the modeled soil and canopy latent heat fluxes to infer soil moisture conditions. On cloudy days, equation 6 is applied directly to predict the fluxes as in the prognostic approach.

[24] The cloud-filling procedure is as follows. For all days (clear or cloudy), hourly fluxes of potential ET are computed for the canopy and soil system components and integrated to daytime totals, $\langle PET_C \rangle$ and $\langle PET_S \rangle$, respectively, where $\langle X \rangle$ indicates the daily integral of quantity X . This step is facilitated by hourly estimates of downwelling solar and longwave radiation, which can be obtained under both clear and cloudy conditions from GOES imagery [Diak et al., 1996, 2000].

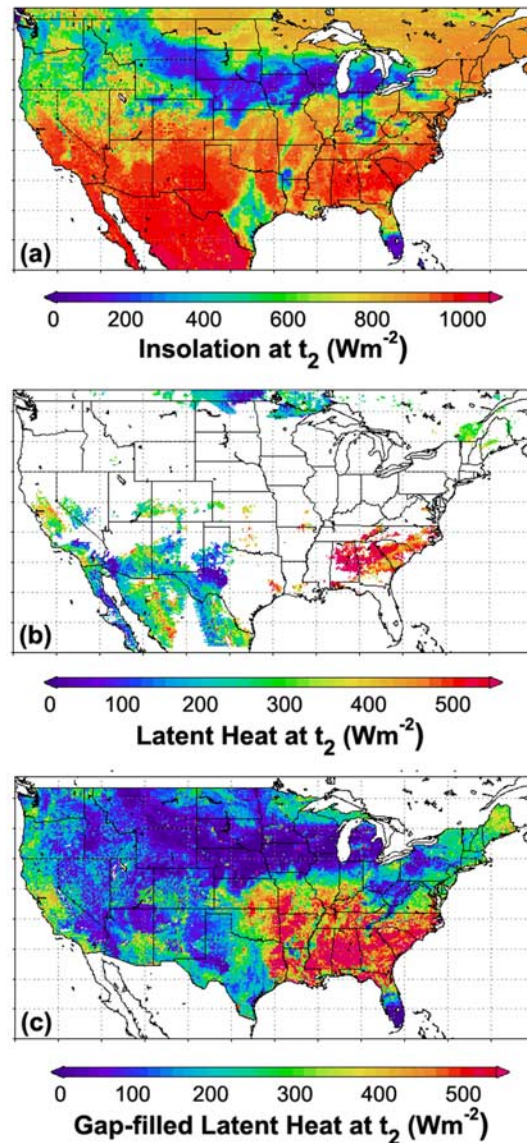


Figure 3. Model fields demonstrating the gap-filling technique as applied to ALEXI output for 30 April 2003: (a) insolation at time t_2 , showing the distribution of cloud cover; (b) latent heat flux estimates at time t_2 for pixels passing the cloud-screen; (c) a cloud-filled field of latent heating at time t_2 .

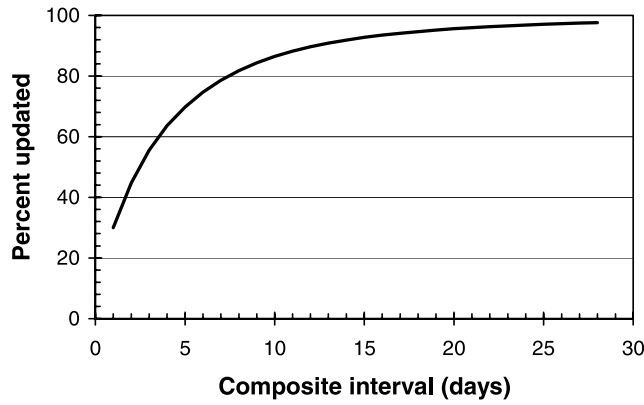


Figure 4. Percent of model domain updated on average as a function of composite time interval.

[25] On clear days, the available water pools AW_{rz} and AW_{sfc} are updated based on the evaporative stress detected in the canopy and soil model components, as reflected in f_{PETc} and f_{PETs} :

$$\begin{aligned} f_{PETc} &= \frac{\langle E_c \rangle}{\langle PET_c \rangle} & f_{PETs} &= \frac{\langle E_s \rangle}{\langle PET_s \rangle} \\ f_{AW_{rz}} &= \text{fn}^{-1}[f_{PETc}] & f_{AW_{sfc}} &= \text{fn}^{-1}[f_{PETs}] \\ AW_{rz} &= f_{AW_{rz}} * AWC_{rz} & AW_{sfc} &= f_{AW_{sfc}} * AWC_{sfc} \\ AW_{rz,next} &= AW_{rz} - \langle E_c \rangle & AW_{sfc,next} &= AW_{sfc} - \langle E_s \rangle \end{aligned} \quad (7)$$

where $\text{fn}^{-1}[f_{PET}]$ is the moisture stress function (equation 6) inverted to solve for f_{AW} . In equation 7, daytime total actual ET fluxes, $\langle E_c \rangle$ and $\langle E_s \rangle$, are extrapolated from instantaneous values at t_2 as described in Appendix C. The final step decrements the moisture pools by that day's water loss to determine AW for the next day.

[26] On cloudy days, these steps are inverted:

$$\begin{aligned} f_{AW_{rz}} &= \frac{AW_{rz}}{AWC_{rz}} & f_{AW_{sfc}} &= \frac{AW_{sfc}}{AWC_{sfc}} \\ f_{PETc} &= \text{fn}[f_{AW_{rz}}] & f_{PETs} &= \text{fn}[f_{AW_{sfc}}] \\ \langle E_c \rangle &= f_{PETc} * \langle PET_c \rangle & \langle E_s \rangle &= f_{PETs} * \langle PET_s \rangle \\ AW_{rz,next} &= AW_{rz} - \langle E_c \rangle & AW_{sfc,next} &= AW_{sfc} - \langle E_s \rangle \end{aligned} \quad (8)$$

This process continues, with daily depletions accounted for, until the next clear day when both surface and root zone moisture pools can be updated.

[27] This gap-filling approach assumes a degree of “self-preservation” [Brutsaert and Sugita, 1992] in the f_{PET} ratio from day to day, after accounting for daily evaporative losses. Brutsaert and Chen [1996] and Porté-Agel et al. [2000] find that the fraction of equilibrium ET (proportional to PET) is more conservative over periods of several days than are other reference flux indices, like the evaporative fraction or the Bowen ratio, when adjusted for soil moisture depletion. The method is insensitive to errors in specification of the Priestley-Taylor coefficient, as long as the coefficient is relatively stable over periods of several days.

[28] A disadvantage to this scheme is that moisture updates will not occur until the first clear day following a precipitation event. In other words, there may be a few days lag before the impact of rainfall over a given pixel is reflected in that pixel's available water pools. On average,

the moisture pools in 75% of the U.S. domain are updated at least once every 6 days, while 95% are updated at least every 20 days (Figure 4). The average frequency of update varies spatially and temporally across the domain according to the regional cloud cover climatology.

[29] A cloud-filled map of instantaneous latent heat flux at time t_2 on 30 April 2003 is shown in Figure 3c. While the cloud-filling algorithm described here is designed for a two-source land-surface model, it could also be easily implemented for a one-source model by maintaining a single moisture pool for the full soil column. The two-source model adds value in that the surface and root-zone pools can be depleted at different rates, as is observed in nature. Note, however, that model sensitivity to the two moisture pools depends on the local vegetation cover fraction. Under high cover conditions, estimates of $f_{AW_{sfc}}$ become more uncertain, and there is little remote sensing information on $f_{AW_{rz}}$ in areas of sparse vegetation. In these extremes, available water estimates from the unsampled pools should be considered indeterminate. Fortunately, the corresponding component PET values will also be low in these areas, so the impact of this loss of information on predicting ET is minimal.

3. Model Input Data

[30] The ALEXI model and associated gap-filling algorithms have been applied over a grid covering the continental U.S. at 10-km resolution and over regional sub-domains associated with specific field experiments at 5-km resolution. Required model input data and operational data sources are listed in Table 1 and described briefly below.

3.1. Surface Radiometric Temperature

[31] The ALEXI model uses two morning observations of surface radiometric temperature acquired at times $t_1 = 1.5$ h and $t_2 = \text{minimum}(5.5 \text{ h past local sunrise, } 1 \text{ h before local noon})$. The minimization constraint on t_2 is imposed to ensure that the assumption of a linear rise in H during the $t_1 - t_2$ time interval (equation A16) is fulfilled over a wide range in latitude.

[32] Brightness temperature data used over the continental domain for 2002–2004 were obtained with the GOES-10 (western US) and -12 (east) Sounder instruments within the 10.2–11.2 μm (Band 4) window, aggregated to a 10-km resolution grid, while data for the 5-km regional grids were acquired from the GOES Imager 10.8 μm channel. GOES view zenith angle varies over the continental U.S. between 25 and 60°. Directional brightness temperature was atmospherically corrected and converted to a radiometric temperature value using a technique described by French et al. [2003], which requires vertical profiles of potential temperature and mixing ratio and an estimate of directional surface emissivity, $\varepsilon(\theta)$. A semi-empirical expression for $\varepsilon(\theta)$ as a function of nominal soil and leaf emissivities (ε_s and ε_c , respectively, currently fixed at 0.94 and 0.97), fractional vegetation cover, and thermal view angle was developed by fitting simulated data created with the Cupid soil-plant-atmosphere model [Norman et al., 1990].

[33] Rigorous flagging of cloud-contaminated pixels is critical to obtaining reasonable flux estimates. Appearance of clouds around time t_2 reduces the apparent surface

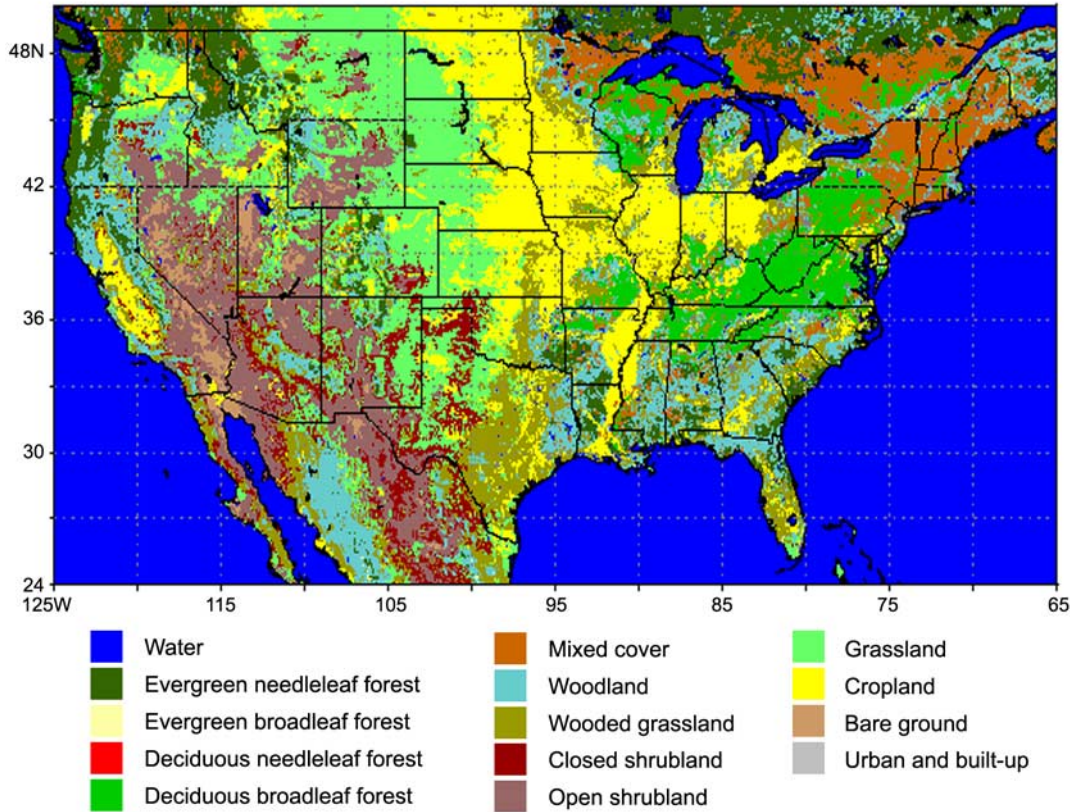


Figure 5. Landcover classification used in ALEXI.

temperature change, mimicking wetter conditions, while clouds at time t_1 augment ΔT_{RAD} and result in high modeled sensible heat rates. Clouds in the intervening period cause non-monotonic fluctuations in sensible heat, in conflict with equation A16. A standard GOES Sounder product (nominally 10-km resolution) quantifying effective cloud amount (CA) using a CO_2 absorption technique [Menzel *et al.*, 1983; Schreiner *et al.*, 2001] was therefore inspected for the time period t_1 to t_2 ; cells are flagged as cloudy if $\text{CA} > 1\%$ at any time during this interval.

3.2. Vegetation Cover Amount

[34] The fraction of vegetation cover apparent at the GOES view angle, $f(\theta)$, was derived from the 1-km MODIS/Terra 8-day composite LAI product from [MOD15A, Collection 4; Myneni *et al.*, 2002] via equation A2. LAI data tiles covering the continental U.S. were mosaicked and reprojected from the MODIS sinusoidal grid to geographic coordinates at 0.01° resolution (~ 1 km) using a nearest neighbor assignment with the MODIS Reprojection Tool. Data at 0.01° were then aggregated to the $\sim 0.09^\circ$ (10 km) ALEXI grid as an unweighted average. To generate daily LAI fields, the 8-day composites were bi-linearly interpolated in time.

3.3. Canopy Characteristics

[35] Satellite-derived fractional cover estimates have been used in conjunction with a gridded land-surface classification to assign relevant surface parameters such as roughness

length and radiometric properties. The current study employs the University of Maryland (UMD) 1-km Global Landcover Product [Hansen *et al.*, 2000], which contains 12 vegetation classes. The dominant landcover class in each 10-km grid cell within the continental model domain is mapped in Figure 5.

[36] Subpixel landcover information at the 1-km scale has been used to estimate aggregate surface parameters for the 5 and 10-km resolution ALEXI model grids. Aggregate values (\bar{x}) of leaf size (used in determining canopy boundary layer resistance, R_x) and leaf absorptivity in the visible, near-infrared, and thermal wave bands (α_{vis} , α_{NIR} , and α_{TIR} ; used in net radiation partitioning, Appendix A) were computed as a weighted average of values expected for each class (x_i ; Table 2):

$$\bar{x} = \frac{\sum_i n_i x_i}{\sum_i n_i} \quad (9)$$

where n_i is the number of 1-km pixels in class i within a given 5 or 10-km ALEXI grid cell. To simulate phenological changes in surface roughness properties, the expected canopy height has been tied to both class and vegetation cover fraction. Within each class, canopy height is scaled linearly with $f(0)$ between a seasonal minimum and maximum value (see Table 2):

$$h_{c,i} = h_{c \min,i} + f(0) [h_{c \max,i} - h_{c \min,i}] \quad (10)$$

Table 2. Landcover Classification Systems Used in the ALEXI and DisALEXI Models, Along With Parameters That Vary According to Landcover Class Including the Seasonal Maximum and Minimum Canopy Heights (h_{\max} and h_{\min}), Leaf Absorptivity (α) in the Visible, NIR, and TIR Bands, and Nominal Leaf Size (s)^a

Class	Description	h_{\min} (m)	h_{\max} (m)	α_{vis}	α_{NIR}	α_{TIR}	s (m)
1	Water	0	0	—	—	—	—
2	Evergreen Needleleaf Forest	15.0	15.0	0.89	0.60	0.95	0.05
3	Evergreen Broadleaf Forest	15.0	15.0	0.87	0.40	0.95	0.10
4	Deciduous Needleleaf Forest	10.0	10.0	0.89	0.60	0.95	0.05
5	Deciduous Broadleaf Forest	10.0	10.0	0.86	0.37	0.95	0.10
6	Mixed Cover	1.0	2.5	0.88	0.51	0.95	0.05
7	Woodland	5.0	5.0	0.87	0.49	0.95	0.05
8	Wooded Grassland	1.0	2.5	0.85	0.36	0.95	0.05
9	Closed Shrubland	0.6	0.6	0.85	0.37	0.95	0.02
10	Open Shrubland	0.5	0.5	0.83	0.35	0.95	0.02
11	Grassland	0.1	0.6	0.82	0.28	0.95	0.02
12	Cropland	0.0	0.6	0.83	0.35	0.95	0.05
13	Bare Ground	0.0	0.2	0.82	0.57	0.95	0.02
14	Urban and Built Up	6.0	6.0	0.84	0.37	0.95	0.02

^aThe ALEXI classification system is based on the UMD 1-km Global Landcover Product [Hansen et al., 2000].

and then the momentum roughness ($z_{0,i}$) and displacement height (d_i) parameters are computed for each class as cover-dependent fractions of the canopy height [Massman, 1997]. Canopy and displacement heights were then aggregated directly via equation 9, whereas area-averaged roughness length, \bar{z}_0 , at the 5 and 10-km scale was determined using the approach of Mason [1988]:

$$\left[\ln \left(\frac{z_b - \bar{d}}{\bar{z}_0} \right) \right]^{-2} = \frac{1}{\sum_i n_i} \sum_i \frac{n_i}{\left[\ln \left(\frac{z_b - d_i}{z_{0,i}} \right) \right]^2} \quad (11)$$

which averages drag coefficients at an effective blending height (z_b , assumed to be at 50 m above ground level; agl) to preserve surface stress in upscaling.

[37] Anderson et al. [2005] demonstrated the impact of vegetation clumping (e.g., as in row crops) on the interpretation of the surface radiometric signature by the TSEB model. Neglect of clumping effects results in a modest overestimation of sensible heating in ALEXI. Here, a nadir clumping index of 0.9 is assumed for the crop land-cover class, while all other classes are assigned a value of 1.0.

3.4. Downwelling Radiation

[38] Downwelling solar and longwave radiation were estimated at each pixel in the ALEXI grid using hourly GOES-based products at 20-km resolution [Diak et al., 1996, 2000]. The upwelling components of net radiation are predicted by the TSEB model itself, based on diagnosed canopy and soil temperatures and estimates of surface emissivity and albedo parameterized primarily in terms of landcover type and vegetation cover fraction (see Appendix A).

[39] Otkin et al. [2005] compared GOES insolation estimates to pyranometer data from 11 sites in the United States Climate Reference Network (USCRN) over a continuous 15-month period. Average root mean square errors of 19% and 10% were obtained for predictions at hourly and daily timesteps, respectively (including both clear and cloudy-sky conditions), which are comparable to the best results that

have reported in the literature for satellite-based radiation algorithms.

3.5. Surface and Upper Air Meteorological Data

[40] Shelter-level wind speed and air temperature data from the U.S. synoptic surface network were analyzed to a 40-km grid using the analysis component of the CIMSS (Cooperative Institute for Meteorological Satellite Studies) Regional Assimilation System (CRAS) mesoscale forecast model [Diak et al., 1992; Wu et al., 1995]. Air temperature is used only in the PET assessments, and the overall model is not very sensitive to this input [Anderson et al., 1997].

[41] Upper-air (radiosonde) data at mandatory and significant levels were also analyzed to the three-dimensional grid of the CRAS, constructed with 40 vertical levels (25 of them below the 600 hPa level in the atmosphere) to preserve a high level of vertical detail in the ABL. These vertical profiles were then interpolated to the ALEXI grid using a nearest neighbor technique as opposed to level-by-level interpolation, which can generate non-physical profiles. Derived lapse rate profiles are used in the ABL submodel, while both temperature and mixing ratio profiles are used to atmospherically correct the GOES brightness temperatures.

3.6. Soil Properties

[42] Gridded available water capacity data have been derived from the State Soil Geographic Database [STATSGO; Miller and White, 1998] 1-km soil texture data set for the continental U.S. (CONUS), which contains 11 soil layers within a total column depth of 2.5 m. The data set was aggregated to the ALEXI grid resolution by identifying the dominant profile within each coarse-scale pixel; nominal AWC values were subsequently computed for the 0–5 cm and 5–200 cm layers, with θ_{wp} and θ_{fc} indexed by texture class (Table 3).

4. Validation of the Gap-Filling Algorithm

[43] Rigorous testing of the gap-filling algorithms described here requires time-continuous flux measurements made at the scale of the ALEXI grid cell. Single towers

Table 3. Soil Moisture Retention Properties Assigned to Each Soil Texture Class

Texture Class	θ_{wp}	θ_{fc}
Sand	0.033	0.091
Loamy Sand	0.055	0.125
Sandy Loam	0.095	0.207
Silt Loam	0.133	0.330
Silt	0.133	0.330
Loam	0.117	0.270
Sandy Clay Loam	0.148	0.255
Silty Clay Loam	0.208	0.366
Clay Loam	0.197	0.318
Sandy Clay	0.239	0.339
Silty Clay	0.250	0.387
Clay	0.272	0.396

cannot adequately sample the variability in fluxes in a heterogeneous landscape at the 5–10 km scale, while flux aircraft provide only snapshots of land-surface conditions at specific points in time [Anderson *et al.*, 2007a]. Spatially and temporally intensive data sets collected during the Soil Moisture Experiment of 2002 (SMEX02) and related Soil Moisture-Atmospheric Coupling Experiment (SMACEX), conducted in June and July in the Walnut Creek (WC) Watershed just south of Ames, Iowa, provide a unique opportunity for direct comparison with regional scale flux predictions and evaluation of gap-filling techniques.

4.1. SMEX02 Validation Data

[44] A reference LAI map over the WC watershed was retrieved from the Normalized Difference Water Index $NDWI = (NIR - SWIR)/(NIR + SWIR)$ [Gao, 1996], computed using 30-m resolution, atmospherically corrected imagery from Landsat 5 Thematic Mapper and Landsat 7 Enhanced Thematic Mapper + (collectively referred to as TM) Bands 4 (near infrared; NIR) and 5 (shortwave infrared; SWIR). The retrieval relationship was developed empirically by Anderson *et al.* [2004a] in comparison with in-situ measurements of LAI, and yields a RMSD of 0.66 at the 30-m scale and a minimal bias (TM-observed) of -0.02 (Figure 6a). TM data were available for mapping LAI on day of year (DOY) 174, 182 and 189, a period of rapid crop growth.

[45] The flux data used for validation were acquired at 10 EC towers in the WC watershed between DOY 167–189 (June 16 to July 8) of 2002. Of these, 5 towers were located in cornfields, and 5 in soybean, proportionally representative of the general cropping census within the WC area for that year [Doraiswamy *et al.*, 2004]. Average tower measurements agreed well with fluxes observed by aircraft flying transects over the watershed, suggesting the network-average flux provided good characterization of watershed-scale fluxes [Anderson *et al.*, 2005]. For more details regarding the SMACEX EC and supporting data, see Prueger *et al.* [2005]. In the flux comparisons presented below, an energy budget closure correction has been applied to the sensible and latent heat flux data, enforcing $H + \lambda E = RN - G$ while preserving the observed Bowen ratio [Twine *et al.*, 2000].

4.2. MODIS Leaf Area Index

[46] Because ET is strongly dependent on vegetation cover amount, it is important to verify that the MODIS LAI product behaves reasonably at the ALEXI grid scale

over the SMACEX timeframe. Figure 6c–f shows a comparison between the MODIS LAI product and TM-derived LAI at 0.01° (~ 1 km, the resolution of the MODIS product), 0.02° , 0.05° , and 0.09° (10 km, the resolution of the continental-scale ALEXI grid) for days 174, 182 and 189 during SMACEX. The MODIS product was bi-linearly interpolated in time between 8-day product dates to the TM imaging dates, and aggregation of both datasets was accomplished through averaging LAI at the highest resolution.

[47] The scatter between MODIS and TM LAI aggregated to 1 km (RMSD ~ 0.7 ; Figure 6c) exceeds that of the TM validation at 30-m resolution (Figure 6a). With increasing pixel scale, the discrepancies between the TM and MODIS LAI estimates progressively diminish. Agreement at 5–10 km resolution (0.05° – 0.09°) is acceptable from a modeling standpoint, with RMSD ~ 0.3 (Figure 6e–f). Averaging over the extent of the watershed domain, the MODIS product reproduces the TM-derived time-behavior well over the period of sampling (Figure 6b).

[48] While the discrepancies at 1-km resolution are large, the Collection 4 MODIS LAI product appears to provide good temporal information regarding LAI at the 5–10 km scale over the WC watershed during SMACEX. The product may be more problematic for other time periods and for other landcover classes, particularly in forest where LAI tends to be overestimated [Fang and Liang, 2005; Wang *et al.*, 2004]. Some of these issues may be addressed in the next LAI product release (Collection 5), using improved retrieval algorithms for woody vegetation [Yang *et al.*, 2005].

4.3. Gap-Filling Techniques

[49] The cloud-filling and daytime-extrapolation algorithms described in Section 2 were applied to ALEXI flux evaluations over a 5-km resolution grid covering the upper Midwest [Anderson *et al.*, 2005]. Figure 7 shows hourly predictions of solar radiation (S_d) and the four major flux components during daylight hours ($S_d > 0$), averaged over the WC domain (4×8 grid cells). The instantaneous values derived directly by ALEXI at time t_2 under clear-sky conditions are indicated in the λE plot (11 points); fluxes at all other times have been gap-filled (265 points). Also shown for reference are hourly flux measurements from SMACEX, representing an average of data from all towers in the WC watershed; a scatterplot representation of these comparisons at hourly and daytime-integrated timescales is provided in Figure 8, with statistical measures in Table 4.

[50] The gap-filling technique appears to provide reasonable estimates of hourly fluxes over this agricultural landscape, reproducing the observed increase in evapotranspiration as the crops mature. The RMSD in the gap-filled estimates of hourly latent heating is 60 Wm^{-2} (19% mean absolute percent difference, MAPD), while combining all flux components yields a RMSD of 48 Wm^{-2} (19% MAPD; Figure 8a). This can be compared to the 30 Wm^{-2} (10%) errors associated with the subset of points generated directly by ALEXI under clear-sky conditions [Anderson *et al.*, 2005]. At the daily timescale, the RMSD for ET is $1.7 \text{ MJm}^{-2} \text{ d}^{-1}$ (11% MAPD) and $1.6 \text{ MJm}^{-2} \text{ d}^{-1}$ (13% MAPD) for all fluxes combined (Figure 8b). The GOES hourly solar radiation product in general provides accurate forcing for the simulations, with a RMSD of 66 Wm^{-2}

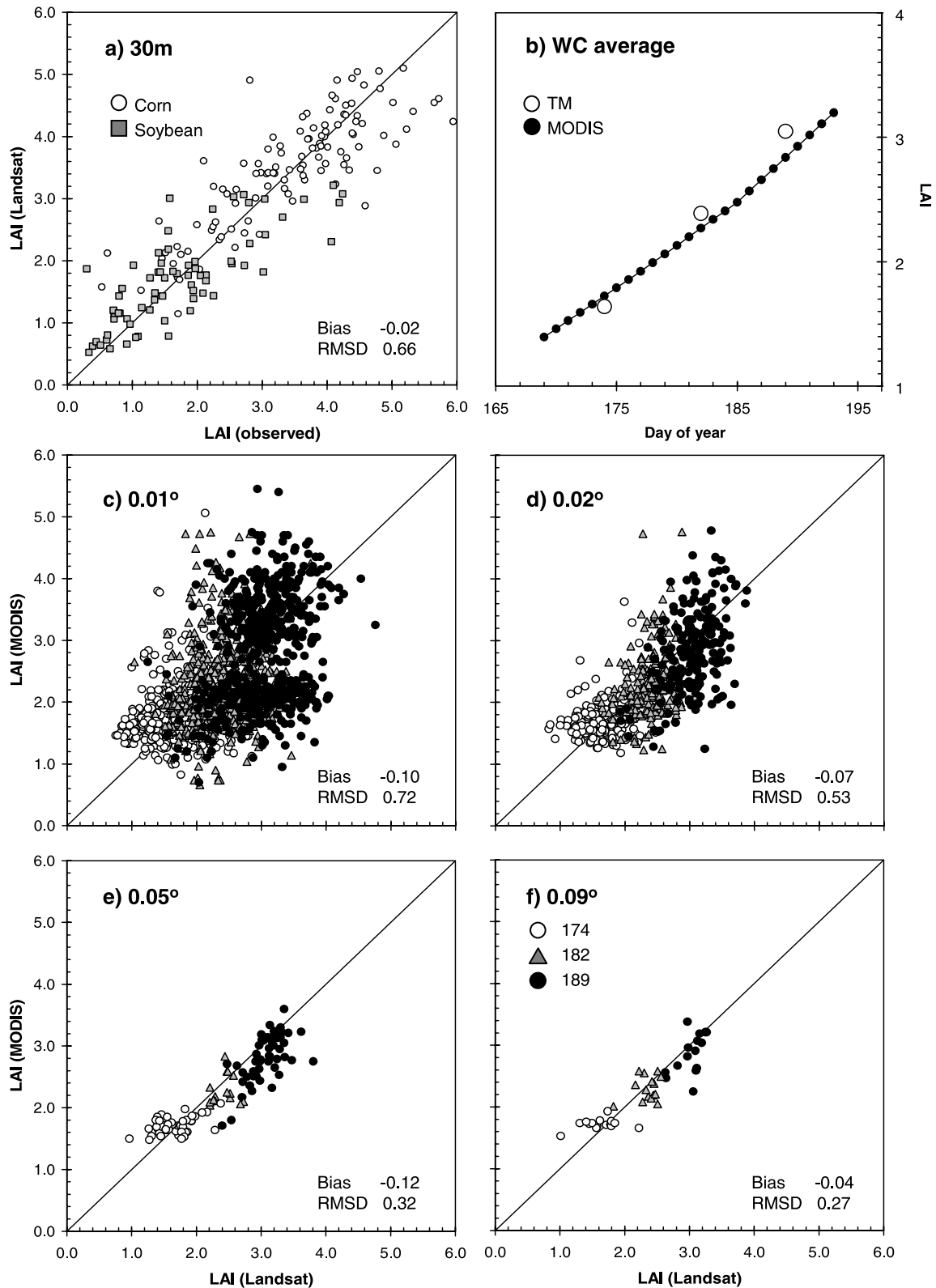


Figure 6. Comparison of MODIS LAI to Landsat TM estimates derived from an empirical regression against ground observations collected during SMEX02: (a) Landsat (30-m resolution) vs. observed LAI; (b) time-evolution of TM and MODIS LAI aggregated to the watershed scale; and MODIS vs. TM LAI aggregated to (c) 0.01°; (d) 0.02°; (e) 0.05°; and (f) 0.09° resolution.

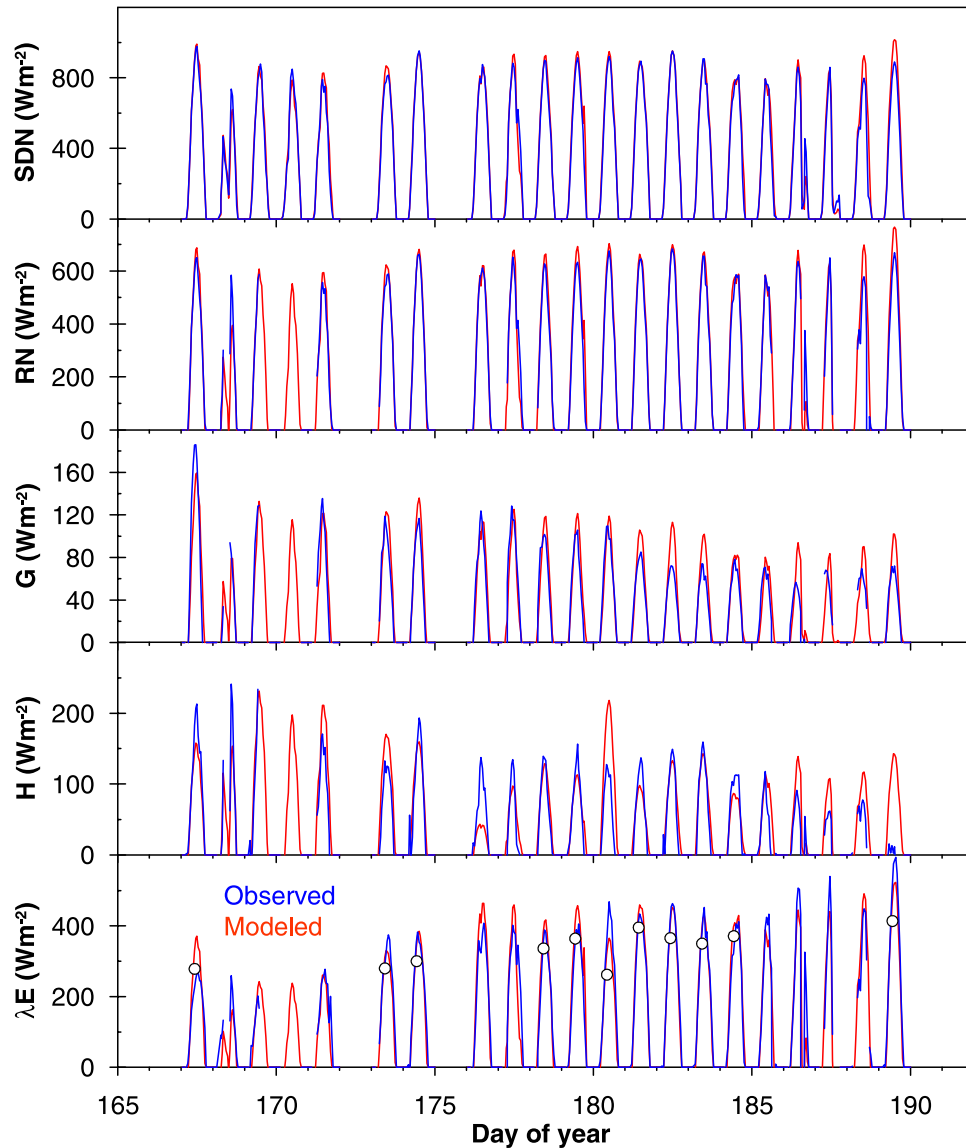


Figure 7. Time series comparison of hourly flux estimates from ALEXI with hourly measurements from the SMEX02 tower network, both averaged over the WC watershed domain. Instantaneous fluxes at time t_2 , generated directly by ALEXI under clear-sky conditions, are indicated in the bottom panel (open circles). All other model fluxes have been gap-filled.

(8% MAPD) with respect to spatially averaged pyranometer readings.

[51] The largest errors in daily sensible and latent heat fluxes occur on DOY 180 and 189 (Figure 7), both purportedly clear days on which ALEXI executed over the WC domain. These days characterize conditions that can be problematic for the ALEXI algorithm, so a review is instructive.

[52] On DOY 180, a cloud band over the watershed at time t_1 went undetected by the GOES cloud mask, resulting in an overestimation of ΔT_{RAD} and therefore H by $\sim 100 \text{ Wm}^{-2}$ midday. Around dawn, the cloud detection product transitions from a nighttime algorithm, focusing on IR bands, to a daytime scheme using visible information [Schreiner *et al.*, 2001]. Under some atmospheric conditions, clouds can occasionally be missed during this transition window [Schreiner, 2005, personal communi-

cation]. Incorporating additional information, for example a comparison of hourly GOES-derived insolation and albedo values with clear-sky estimates, may improve early morning cloud detection.

[53] ALEXI predicts positive sensible heat fluxes peaking at 140 Wm^{-2} on DOY 189, while fluxes observed on the ground were small in the morning and went negative midday. The cause of this discrepancy is two-fold. First, the GOES-based insolation algorithm overestimated insolation on DOY 188–189, presumably due to increased atmospheric aerosol content carried by smoke from an outbreak of forest fires in the western U.S. [Walthall *et al.*, 2004]. Net radiation was likewise overestimated, increasing all components of the modeled surface energy budget. Furthermore, tower-based measurements showed afternoon shelter-level air temperature exceeding surface temperature,

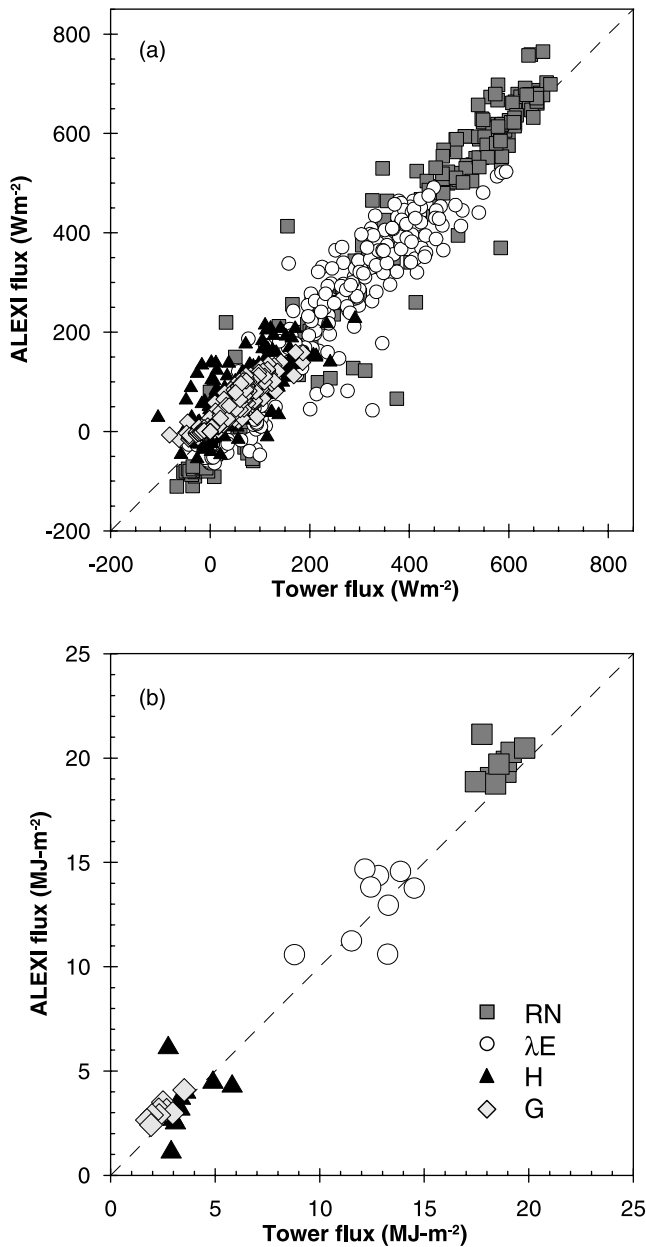


Figure 8. Scatterplot comparison of modeled and measured watershed-average fluxes from SMEX02 at (a) hourly and (b) daily timesteps.

a sign of local warm-air advection likely driving the negative sensible heat fluxes [Li *et al.*, 2006]. Effects of horizontal advection are not currently included in the ABL growth submodel in ALEXI, but can be incorporated using the techniques of Diak and Whipple [1993], using a comparison between temperature soundings at 0 and 12 UTC or simulated soundings from a mesoscale forecast model.

4.4. Available Water Fraction

[54] ALEXI-derived partitioning of soil moisture between the root-zone and soil surface is demonstrated in Figure 9, showing a time history of modeled AWF_{rz} and AWF_{sfc} during SMEX02, averaged over the WC study domain. Also shown are the timing and magnitudes of local precipitation

events, as measured on average by the WC rain gauge network. Dates when the domain was predominantly clear and area-averaged soil moisture pools were updated by ALEXI are indicated; AWF values during intervening cloudy intervals were filled as discussed above.

[55] The ALEXI-derived available water fraction, particularly in the surface layer, responds to the major rainfall event occurring on DOY 191. The modeled response, however, is delayed until the first clear day following the event (DOY 194), when the surface can again be viewed by the satellite sensors. The surface then dries rapidly over the next two days (both clear, and thus directly modeled by ALEXI), as would be expected. Warm-air advection on DOY 189 caused the model to underestimate the observed latent heating, resulting in an under-prediction of AWF_{sfc} on this day and masking the impact of the minor rainfall events on DOY 185–187.

[56] Prior to the rainfall event on DOY 191 there is a slow depletion in the modeled root-zone soil moisture (the noise spike on DOY 180 is due to incomplete cloud clearing as described in the previous section). While there was stress-induced leaf curl observed at the margins of some corn fields during this dry-down period, the vegetation stress at the watershed scale represented by these model results was likely only moderate. The model estimates a 20% reduction in canopy transpiration due to stress by DOY 190.

[57] In general, the gross response of model-predicted soil moisture to antecedent precipitation over the WC watershed is reasonable. Due in part to decreasing sensitivity to the soil surface temperature as the crop canopy closes, predictions of AWF_{sfc} exhibit higher noise than do those of AWF_{rz} ; the opposite would likely be the case under low vegetation cover conditions. Still, it is encouraging that there appears to be a detectable thermal signal of increased soil surface moisture associated with this rainfall event even under relatively dense vegetation cover ($LAI \sim 3$; Figure 6b).

5. Conclusions and Future Research

[58] A strategy has been presented for computing time-continuous fluxes over continental scales using thermal remote sensing data from a geostationary satellite platform. This strategy fills flux estimates during gaps in the remote sensing record because of intermittent cloud cover. It is assumed that the fraction of potential ET (f_{PET}) derived on clear days is conserved (minus evaporative depletion of soil moisture resources) until the next clear day. On clear days, f_{PET} is mapped to an available water fraction (AWF); on cloudy days, this mapping is inverted to predict the evaporative fluxes. At the end of each day, the current AWF is depleted by that day's evaporative extractions.

[59] The gap-filling methodology uses a two-source model of the land-surface energy balance (TSEB), which partitions system fluxes between the soil and vegetated components of the modeling scene and allows differential adjustment of moisture pools in the soil surface and root zone layers, which have very different time constants in terms of moisture release. The rapid soil evaporation that occurs right after rainfall can be differentiated from the longer term trends in the root zone, which are more directly tied to crop health and projected yield. This gap-filling strategy could be easily adapted for use with single-source

Table 4. Quantitative Measures of ALEXI Model Performance^a in Estimating WC-Average Tower Fluxes

Flux	N	\overline{O} W m ⁻²	MBE W m ⁻²	RMSD W m ⁻²	% Error
<i>Hourly</i>					
RN	265	342	10	60	12
G	265	54	8	21	31
H	265	69	13	44	48
LE	265	233	-11	58	19
All	1060	174	5	48	19
<i>Daily</i>					
RN	10	18.6	1.4	1.4	7
G	10	2.3	0.7	0.8	31
H	10	3.2	0.6	2.1	43
LE	10	13.0	0.15	1.7	11
All	40	9.3	0.7	1.6	13

^aHere N is the number of observations, \overline{O} is the mean observed flux, RMSD is the root-mean square difference between the modeled (P) and observed (O) quantities, MBE is the mean-bias-error ($\overline{P} - \overline{O}$), and the percent error is defined as the mean-absolute-difference between P and O divided by the mean observed flux.

energy balance models by linking to a single moisture pool describing the bulk soil profile. However, the dynamic interactions between soil moisture and ET may not be as well represented by such a system.

[60] When coupled with an ABL growth model to provide atmospheric temperature boundary conditions, the TSEB can be executed over regional scales. The resulting ALEXI model and gap-filling techniques were applied to a 2-week data set collected during the SMACEX/SMEX02 field experiments, where a high density tower network and associated aircraft flights allowed good characterization of fluxes at the watershed scale. Continuous, gap-filled predictions agreed with watershed-average tower measurements to within 19% for hourly fluxes and 13% for daytime totals. The highest errors were incurred on days when the early-morning cloud mask failed to detect cloud-contaminated thermal pixels, and when strong warm-air advection reduced observed sensible heat flux to negative values by midday.

[61] The time behavior of modeled available water fraction, in the root zone and in the soil surface layer, was qualitatively examined in comparison with precipitation measurements. The modeled moisture in the surface layer (top 5 cm) responds quickly to major rainfall events and then quickly subsides, whereas root-zone moisture changes are more gradual during a dry-down period, as expected. In

future studies, these responses will be evaluated quantitatively in comparison with extensive ground-based measurements and microwave-derived soil moisture maps that were collected during SMEX02 and with measurements from Soil Climate Analysis Network (SCAN). Work is underway to evaluate the utility of ALEXI thermal-based soil moisture predictions in terms of assimilation into prognostic hydrologic models [Crow *et al.*, 2005] and initialization of meso-scale forecast models [Hain *et al.*, 2005b]. Assessments using data from the Oklahoma Mesonet have demonstrated that ALEXI has considerable skill in retrieving volumetric soil moisture content in comparison with fields from the Eta Data Assimilation System [EDAS; Hain *et al.*, 2005a].

[62] This exercise has identified several aspects of the ALEXI modeling system that can be refined in future studies. Better cloud-screening and atmospheric correction algorithms should reduce noise in daily flux evaluations by improving the ΔT_{RAD} signal. In addition, a correction for horizontal advection of temperature can be assessed using a mesoscale forecast model, this will be especially important in regions of mountainous terrain. The soil moisture and moisture stress fields from ALEXI require further validation in other ecological and climatic systems to demonstrate general utility. Localized studies with the TSEB can be used to tune the shape of the crop and soil stress functions to

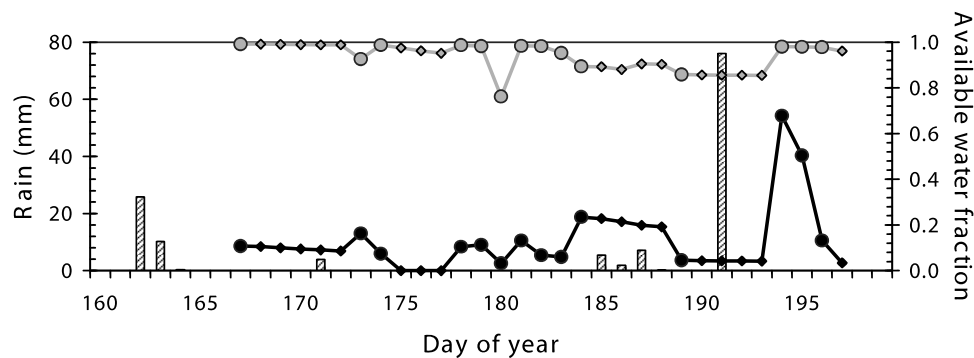


Figure 9. Available water fraction estimates from ALEXI for the root zone (grey line) and soil surface layer (black line) vs. DOY, averaged over the WC watershed. Larger symbols indicate values generated by the clear-sky algorithm in ALEXI; all other values were gap-filled. Also, shown are daily watershed-averaged precipitation rates.

better represent the temporal evolution of surface and root-zone moisture measurements.

[63] The ALEXI land-surface modeling framework has been applied to GOES thermal imagery collected over the continental U.S. from 2002 to 2004. The results of a 3-year climatological study of surface moisture and evaporative conditions over the U.S. are presented in a companion paper (A2).

Appendix A: The ALEXI Model

[64] The surface boundary conditions in ALEXI are provided by the TSEB model [Norman *et al.*, 1995], which extracts soil and canopy temperatures (T_s and T_c) from composite directional surface radiometric temperature ($T_{\text{RAD}}(\theta)$) measurements acquired by satellite:

$$T_{\text{RAD}}(\theta) \cong f(\theta)T_c + [1 - f(\theta)]T_s \quad (\text{A1})$$

where $f(\theta)$ is the fractional cover:

$$f(\theta) = 1 - \exp\left(\frac{-0.5\Omega(\theta)F}{\cos \theta}\right) \quad (\text{A2})$$

F is the leaf area, and $\Omega(\theta)$ is the vegetation clumping factor apparent at view angle θ [Anderson *et al.*, 2005].

[65] In TSEB, equations A1 and A2 are solved simultaneously with a set of equations describing the surface energy budget for the soil, canopy, and composite land-surface system:

System, soil, and canopy energy budgets:

$$RN = H + \lambda E + G \quad (\text{A4})$$

$$RN_S = H_S + \lambda E_S + G \quad (\text{A5})$$

$$RN_C = H_C + \lambda E_C \quad (\text{A6})$$

Net radiation:

$$RN = RN_S + RN_C \quad (\text{A7})$$

$$\begin{aligned} RN &= (L_d - L_u) + (S_d - S_u) \\ &= L_d - (1 - \tau_c)L_c - \tau_c L_s + (1 - A)S_d \end{aligned} \quad (\text{A8})$$

$$\begin{aligned} RN_S &= (L_{d,s} - L_{u,s}) + (S_{d,s} - S_{u,s}) \\ &= \tau_c L_d + (1 - \tau_c)L_c - L_s + (1 - \rho_s)S_{d,s} \end{aligned} \quad (\text{A9})$$

Sensible heat:

$$H = H_S + H_C = \rho_c p \frac{T_{AC} - T_A}{R_A} \quad (\text{A10})$$

$$H_S = \rho_c p \frac{T_S - T_{AC}}{R_S} \quad (\text{A11})$$

$$H_C = \rho_c p \frac{T_C - T_{AC}}{R_X} \quad (\text{A12})$$

Latent heat:

$$\lambda E = \lambda E_S + \lambda E_C \quad (\text{A13})$$

$$\lambda E_C = \alpha_c f_g \frac{\Delta}{\Delta + \gamma} RN_C \quad (\text{A14})$$

Soil conduction heat:

$$G = \alpha_g RN_S \quad (\text{A15})$$

Here RN is net radiation, H is sensible heat, λE is latent heat, G is the soil heat conduction flux, T is temperature, R is a transport resistance, ρ is air density, c_p is the heat capacity of air at constant pressure, γ is the psychrometric constant, and Δ is the slope of the saturation vapor pressure vs. temperature curve. The subscripts 'A', 'AC', and 'X' signify properties of the air above and within the canopy, and within the leaf boundary layer, respectively, while 'S' and 'C' refer to fluxes and states associated with the soil and canopy components of the system. The soil heat conduction flux is computed as a fraction α_g of the net radiation below the canopy, at the soil surface [equation A15; Choudhury *et al.*, 1987], with $\alpha_g = 0.31$ typical of values derived from mid-morning flux observations, the period when ALEXI is applied [Kustas *et al.*, 1998]. In equation A14, transpiration is tied to the net radiation divergence in the canopy (RN_C) through a modified Priestley-Taylor relationship [Priestley and Taylor, 1972], where α_c is a coefficient with a nominal value of 1.3 that is downward-adjusted if signs of vegetative stress are detected (see main text) and f_g is the fraction of green vegetation in the scene. Justification for this parameterization of λE_C is provided by Norman *et al.* [1995].

[66] The series resistance formalism described here allows both the soil and the vegetation to influence the microclimate within the canopy air space, as shown in Figure 1. The resistances considered include R_A , the aerodynamic resistance for momentum between the canopy and the upper boundary of the model (including diabatic corrections); R_X , the bulk boundary layer resistance over all leaves in the canopy; and R_S , the resistance through the boundary layer immediately above the soil surface. Mathematical expressions for these resistance terms are given by Norman *et al.* [1995].

[67] In equations A1–15, RN is the net radiation above the canopy, RN_C is the component absorbed by the canopy, and RN_S is the component penetrating to the soil surface. The longwave components of RN and RN_S are a function of the thermal radiation from the sky (L_d), the canopy (L_c) and the soil (L_s), and the coefficient of diffuse radiation transmission through the canopy (τ_c). The shortwave components depend on insolation values above the canopy (S_d) and above the soil surface ($S_{d,s}$), and the reflectivity of the soil-canopy system (A) and the soil surface itself (ρ_s). Based on the work of Goudriaan [1977], Campbell and Norman [1998] provide analytical approximations for τ_c and A for sparse to deep canopies, depending on leaf absorptivity in the visible, near-infrared and thermal bands, ρ_s , and leaf area index [see Appendix B in Anderson *et al.*, 2000 for further information].

[68] The ALEXI model uses an atmospheric boundary layer (ABL) closure technique to evaluate the morning evolution of air temperature, T_a , in the surface layer. Using radiometric temperature data at times t_1 and t_2 (about 1.5 and 5.5 h past local sunrise) and initial estimates of air temperature, the TSEB surface model component of ALEXI (equations A1–A15) computes instantaneous sensible heat flux estimates H_1 and H_2 . Assuming a linear functional form for $H(t)$ during this morning interval, a time-integrated heat flux can be obtained:

$$\int_{t_1}^{t_2} H(t) dt = \frac{1}{2} [H_2 t_2 - H_1 t_1]. \quad (\text{A16})$$

McNaughton and Spriggs [1986] give a conservation equation relating the rise in height (z) and potential temperature (θ_m) of the mixed layer to the time-integrated sensible heating from the surface:

$$\int_{t_1}^{t_2} H(t) dt = \rho c_p (z_2 \theta_{m2} - z_1 \theta_{m1}) - \rho c_p \int_{z_1}^{z_2} \theta_s(z) dz, \quad (\text{A17})$$

where $\theta_s(z)$ represents an early morning ABL potential temperature sounding. Near the land surface, the mixed layer potential temperature and the air temperature are related by

$$\theta_m = T_a \left(\frac{100}{p} \right)^{R/c_p} \quad (\text{A18})$$

where p is the atmospheric pressure (in kPa) and $R/c_p = 0.286$. Because differential surface temperature measurements are more reliable than absolute temperature measurements, in practice z_1 (the ABL height at time t_1) is fixed at some small value (50 m), and the *change* in modeled θ_m is to allowed to govern the ABL growth based on the lapse rate profile above z_1 [as opposed to diagnosing both z_1 and z_2 ; see Anderson *et al.*, 1997]. While this equation A17 represents a very simplified treatment of entrainment, McNaughton and Spriggs [1986] found that it produces reasonable values of simulated ET, although boundary layer height z_2 is sometimes greatly overestimated. The surface and boundary layer components of the model iterate until the time-integrated sensible heat flux estimates from both components converge. Anderson *et al.* [1997] provide further details concerning the solution sequence used in the ALEXI model.

Appendix B: Potential Evapotranspiration

[69] Potential canopy transpiration is computed using the Priestley-Taylor approximation applied to the net radiation divergence in the canopy [Norman *et al.*, 1995; Tanner and Sinclair, 1983], similar to the initial estimate used in the TSEB (equation A14) but in units of water amount (mm s^{-1}):

$$\text{PET}_c = \frac{\alpha_c}{\lambda} f_g \frac{\Delta}{\Delta + \gamma} \text{RN}_c \quad (\text{B1})$$

where $\alpha_c = 1.3$.

[70] Potential soil evaporation is estimated following Tanner and Jury [1976], again with a modified PT approximation. Tanner and Jury argue that under full canopy cover, a soil PT coefficient (α_s) of 1 should be used to describe soil evaporation, because the airspace above the soil will become almost fully saturated and evaporation will approach the equilibrium value. For bare soil conditions, however, α_s should approach a potential value of 1.3. Between these endpoints, the coefficient depends on the value of a canopy transmission factor:

$$\tau = \exp\left(-0.45F/\sqrt{2 \cos \phi_s}\right) \quad (\text{B2})$$

where ϕ_s is the solar zenith angle, in comparison with a critical value $\tau_{\text{crit}} = 0.5$:

$$\begin{aligned} \text{for } \tau \leq \tau_{\text{crit}}, \alpha_s &= 1 \\ \text{for } \tau > \tau_{\text{crit}}, \alpha_s &= \alpha_c - \left[\frac{(\alpha_c - 1)(1 - \tau)}{(1 - \tau_{\text{crit}})} \right]. \end{aligned} \quad (\text{B3})$$

Then

$$\text{PET}_s = \frac{\alpha_s}{\lambda} \frac{\Delta}{\Delta + \gamma} \text{RN}_s. \quad (\text{B4})$$

Hourly values of RN_c , RN_s , PET_c and PET_s are obtained using GOES-based downwelling short- and long-wave radiation products [Diak *et al.*, 1996, 2000], which can be evaluated at up to 15-minute intervals under both clear and cloudy conditions.

Appendix C: Extrapolation From Instantaneous to Hourly and Daily Fluxes

[71] A common technique for extrapolating instantaneous satellite-based flux estimates to daily totals is to assume that the evaporative fraction (EF), given by the ratio of latent heat to the available energy, is constant during daylight hours for a given day [Gurney and Hsu, 1990; Shuttleworth *et al.*, 1989; Sugita and Brutsaert, 1991]. Given the value of EF determined at the ALEXI modeling time (t_2) along with hourly estimates of RN and G at times t_i , which can be obtained from GOES, hourly values of system sensible and latent heating can be computed for days with clear mornings as:

$$\begin{aligned} \lambda E_i &= EF(\text{RN}_i - G_i) \\ H_i &= \text{RN}_i - G_i - \lambda E_i. \end{aligned} \quad (\text{C1})$$

Previous studies have shown that daily total fluxes estimated using the EF measured at midday underestimate observed totals by 5–10% [Brutsaert and Sugita, 1992; Crago, 1996; Gurney and Hsu, 1990; Sugita and Brutsaert, 1991; Zhang and Lemeur, 1995], therefore EF is defined here as

$$EF = 1.1 \frac{\lambda E_2}{\text{RN}_2 - G_2} \quad (\text{C2})$$

using flux components computed at modeling time t_2 .

[72] For clear pixels, hourly fluxes from the soil component of the two-source system are obtained as

$$\begin{aligned} EF_S &= 1.1 \frac{\lambda E_{S2}}{RN_{S2} - G_2} \\ \lambda E_{Si} &= EF_S (RN_{Si} - G_i) \\ H_{Si} &= RN_{Si} - G_i - \lambda E_{Si} \end{aligned} \quad (C3)$$

while the canopy components are determined as residuals:

$$\begin{aligned} \lambda E_{Ci} &= \lambda E_i - \lambda E_{Si} \\ H_{Ci} &= H_i - H_{Si} \end{aligned} \quad (C4)$$

(similar results are obtained by computing soil fluxes as the residual). Hourly E_{Ci} and E_{Si} are integrated to provide the daily total water extractions $\langle E_C \rangle$ and $\langle E_S \rangle$ used to update the root-zone and soil surface moisture pools (equation 7).

[73] For cloudy pixels, hourly values of latent heat flux are simply estimated from hourly PET_i and contemporaneous stress function values, while sensible heat is computed as a residual to the component energy budget:

$$\begin{aligned} E_{Ci} &= f_{PETc} * PET_{Ci} & E_{Si} &= f_{PETs} * PET_{Si} \\ H_{Ci} &= RN_{Ci} - E_{Ci} & H_{Si} &= RN_{Si} - E_{Si} - G_i \end{aligned} \quad (C5)$$

[74] **Acknowledgments.** This work was supported by the NASA EOS and Land Surface Hydrology Programs. In particular, funding for this research was provided primarily by NASA grant NAG13-99008 and in part by USDA Cooperative Agreement 58-1265-1-043.

References

- Abramopoulos, F., C. Rosenzweig, and B. Choudhury (1988), Improved ground hydrology calculations for global climate models (GCMs): Soil water movement and evapotranspiration, *J. Climate Appl. Meteorol.*, **1**, 921–941.
- Anderson, M. C., J. M. Norman, G. R. Diak, W. P. Kustas, and J. R. Mecikalski (1997), A two-source time-integrated model for estimating surface fluxes using thermal infrared remote sensing, *Remote Sens. Environ.*, **60**, 195–216.
- Anderson, M. C., J. M. Norman, T. P. Meyers, and G. R. Diak (2000), An analytical model for estimating canopy transpiration and carbon assimilation fluxes based on canopy light-use efficiency, *Agric. For. Meteorol.*, **101**, 265–289.
- Anderson, M. C., C. M. U. Neale, F. Li, J. M. Norman, W. P. Kustas, H. Jayanthi, and J. Chavez (2004a), Upscaling ground observations of vegetation water content, canopy height, and leaf area index during SMEX02 using aircraft and Landsat imagery, *Remote Sens. Environ.*, **92**, 447–464.
- Anderson, M. C., J. M. Norman, J. R. Mecikalski, R. D. Torn, W. P. Kustas, and J. B. Basara (2004b), A multi-scale remote sensing model for disaggregating regional fluxes to micrometeorological scales, *J. Hydrometeorol.*, **5**, 343–363.
- Anderson, M. C., J. M. Norman, W. P. Kustas, F. Li, J. H. Prueger, and J. M. Mecikalski (2005), Effects of vegetation clumping on two-source model estimates of surface energy fluxes from an agricultural landscape during SMACEX, *J. Hydrometeorol.*, **6**, 892–909.
- Anderson, M. C., W. P. Kustas, and J. M. Norman (2007a), Upscaling tower and aircraft fluxes from local to continental scales using thermal remote sensing, *Agron. J.*, **99**, 240–254.
- Anderson, M. C., J. M. Norman, J. R. Mecikalski, J. P. Otkin, and W. P. Kustas (2007b), A climatological study of evapotranspiration and moisture stress across the continental U.S. based on thermal remote sensing: II. Surface moisture climatology, *J. Geophys. Res.*, doi:10.1029/2006JD007507, in press.
- Arnold, J. G., R. Srinivasan, R. S. Muttiah, and J. R. Williams (1998), Large area hydrologic modeling and assessment. Part I: Model development, *J. Amer. Water Resour. Assoc.*, **34**, 73–89.
- Bastiaanssen, W. G. M., M. Menenti, R. A. Feddes, and A. A. M. Holtslag (1998), A remote sensing surface energy balance algorithm for land (SEBAL): 1. Formulation, *J. Hydrol.*, **212**–**213**, 198–212.
- Beljaars, A., P. Viterbo, M. Miller, and A. Betts (1996), The anomalous rainfall over the US during July 1993 — sensitivity to land-surface parameterization and soil moisture, *Monthly Weather Rev.*, **124**, 362–383.
- Betts, A. K., F. Chen, K. E. Mitchell, and Z. I. Janjic (1997), Assessment of the land surface and boundary layer models in two operational versions of the NCEP Eta model using FIFE data, *Mon. Weather Rev.*, **125**, 2896–2916.
- Brutsaert, W. (1984), *Evaporation into the atmosphere: theory, history and applications*, D. Reidel, Boston.
- Brutsaert, W., and D. Chen (1995), Desorption and the two stages of drying of natural tallgrass prairie, *Water Resources Res.*, **31**, 1305–1313.
- Brutsaert, W., and D. Chen (1996), Diurnal variation of surface fluxes during thorough drying (or severe drought) of natural prairie, *Water Resources Res.*, **32**, 2013–2019.
- Brutsaert, W., and M. Sugita (1992), Application of self-preservation in the diurnal evolution of the surface energy budget to determine daily evaporation, *J. Geophys. Res.*, **97**, 18,377–18,382.
- Campbell, G. S., and J. M. Norman (1998), *An introduction to environmental biophysics*, Springer-Verlag, New York.
- Capehart, W. J., and T. N. Carlson (1997), Decoupling of surface and near-surface soil water content: A remote sensing perspective, *Water Resources Res.*, **33**, 1383–1395.
- Carlson, T. N., R. R. Gillies, and T. J. Schmugge (1995), An interpretation of methodologies for indirect measurement of soil water content, *Agric. For. Meteorol.*, **77**, 191–205.
- Chen, F., K. Mitchell, J. Schaake, Y. Xue, H. Pan, V. Koren, Q. Y. Duan, M. Ek, and A. Betts (1996), Modeling of land surface evaporation by four schemes and comparison with FIFE observations, *J. Geophys. Res.*, **101**, 7251–7268.
- Choudhury, B. J., S. B. Idso, and R. J. Reginato (1987), Analysis of an empirical model for soil heat flux under a growing wheat crop for estimating evaporation by an infrared-temperature-based energy balance equation, *Agric. For. Meteorol.*, **39**, 283–297.
- Crago, R. D. (1996), Comparison of the evaporative fraction and the Priestley-Taylor α for parameterizing daytime evaporation, *Water Resources Res.*, **32**, 1403–1409.
- Crow, W. T., F. Li, and W. P. Kustas (2005), Intercomparison of spatially distributed models for predicting surface energy flux patterns during SMACEX, *J. Hydrometeorology*, 941–953.
- Diak, G. R., and M. S. Whipple (1993), Improvements to models and methods for evaluating the land-surface energy balance and ‘effective’ roughness using radiosonde reports and satellite-measured skin temperature data, *Agric. For. Meteorol.*, **63**, 189–218.
- Diak, G. R., D. Kim, M. S. Whipple, and X. Wu (1992), Preparing for the AMSU, *Bull. Amer. Meteor. Soc.*, **73**, 1971–1984.
- Diak, G. R., W. L. Bland, and J. R. Mecikalski (1996), A note on first estimates of surface insolation from GOES-8 visible satellite data, *Agric. For. Meteorol.*, **82**, 219–226.
- Diak, G. R., W. L. Bland, J. R. Mecikalski, and M. C. Anderson (2000), Satellite-based estimates of longwave radiation for agricultural applications, *Agric. For. Meteorol.*, **103**, 349–355.
- Diak, G. R., J. R. Mecikalski, M. C. Anderson, J. M. Norman, W. P. Kustas, R. D. Torn, and R. L. DeWolf (2003), Estimating land-surface energy budgets from space: Review and current efforts at the University of Wisconsin-Madison and USDA-ARS, *Bull. Amer. Meteorol. Soc.*, **85**, 65–78.
- Doraiswamy, P. C., J. L. Hatfield, T. J. Jackson, B. Akhmedoc, J. Prueger, and A. Stern (2004), Crop condition and yield simulations using Landsat and MODIS, *Remote Sens. Environ.*, **92**, 548–559.
- Fang, H., and S. Liang (2005), A hybrid inversion method for mapping leaf area index from MODIS data: experiments and application to broadleaf and needleleaf canopies, *Remote Sens. Environ.*, **94**, 405–424.
- France, J., and J. H. M. Thornley (1984), *Mathematical Models in Agriculture*, 335 pp., Butterworths and Co., London.
- French, A. N., J. M. Norman, and M. C. Anderson (2003), A simple and fast atmospheric correction for spaceborne remote sensing of surface temperature, *Remote Sens. Environ.*, **87**, 326–333.
- Gao, B. (1996), NDWI — A normalized difference water index for remote sensing of vegetation liquid water from space, *Remote Sens. Environ.*, **58**, 257–266.
- Gillies, R. R., J. Cui, T. N. Carlson, W. P. Kustas, and K. S. Humes (1997), Verification of a method for obtaining surface soil water content and energy fluxes from remote measurements of NDVI and surface radiant temperature, *Int. J. Remote Sens.*, **18**, 3145–3166.
- Goudriaan, J. (1977), *Crop micrometeorology: a simulation study*, Simulation Monographs, Wageningen.
- Gurney, R. J., and A. Y. Hsu (1990), Relating evaporative fraction to remotely sensed data at the FIFE site, paper presented at Symposium on FIFE: First ISLSCP Field Experiment, Boston, MA, February 7–9, 1990.

- Hain, C. R., J. R. Mecikalski, and M. C. Anderson (2005a), Validation of ALEXI-derived volumetric soil moisture over the continental United States, paper presented at American Meteorological Society.
- Hain, C. R., J. R. Mecikalski, M. C. Anderson, and W. Lapenta (2005b), Initialization of a numerical mesoscale model with ALEXI-derived volumetric soil moisture observations, paper presented at American Meteorological Society.
- Hansen, M. C., R. S. Defries, J. R. G. Townshend, and R. Sohlberg (2000), Global land cover classification at 1 km spatial resolution using a classification tree approach, *Int. J. Remote Sens.*, **21**, 1331–1364.
- Kim, J., and S. B. Verma (1990), Components of surface energy balance in a temperate grassland ecosystem, *Boundary-Layer Meteorol.*, **51**, 401–417.
- Kustas, W. P., and J. M. Norman (1999), Evaluation of soil and vegetation heat flux predictions using a simple two-source model with radiometric temperatures for partial canopy cover, *Agric. For. Meteorol.*, **94**, 13–25.
- Kustas, W. P., and J. M. Norman (2000), A two-source energy balance approach using directional radiometric temperature observations for sparse canopy covered surfaces, *Agronomy J.*, **92**, 847–854.
- Kustas, W. P., G. R. Diak, and J. M. Norman (2001), Time difference methods for monitoring regional scale heat fluxes with remote sensing, *Land Surface Hydrology, Meteorology, and Climate: Observations and Modeling*, **3**, 15–29.
- Kustas, W. P., J. Hatfield, and J. H. Prueger (2005), The Soil Moisture Atmosphere Coupling Experiment (SMACEX): Background, Hydrometeorological Conditions and Preliminary Findings, *J. Hydrometeorol.*, **6**, 791–804.
- Kustas, W. P., Z. Zhang, and T. J. Schmugge (1998), Combining optical and microwave remote sensing for mapping energy fluxes in a semiarid watershed, *Remote Sens. Environ.*, **64**, 116–131.
- Kustas, W. P., M. C. Anderson, A. N. French, and D. Vickers (2006), Using a remote sensing field experiment to investigate flux footprint relations and flux sampling distributions for tower and aircraft-based observations, *Adv. Water Res.*, **29**, 355–368.
- Li, F., W. P. Kustas, M. C. Anderson, T. J. Jackson, R. Bindlish, and J. Prueger (2006), Comparing the utility of microwave and thermal remote-sensing constraints in two-source energy balance modeling over an agricultural landscape, *Remote Sens. Environ.*, **101**, 315–328.
- Liang, X., D. P. Lettenmaier, E. F. Wood, and S. J. Burges (1994), A simple hydrologically based model of land surface water and energy fluxes for GSMs, *J. Geophys. Res.*, **99**(D7), 14,415–14,428.
- Mahfouf, J. F., and J. Noilhan (1991), Comparative study of various formulations of evaporation from bare soil using in situ data, *J. Appl. Meteorol.*, **30**, 1354–1365.
- Mahrt, L., and H.-L. Pan (1984), A two layer model for soil hydrology, *Bound.-Layer Meteorol.*, **29**, 1–20.
- Mason, P. J. (1988), The formation of areally-averaged roughness lengths, *Q. J. R. Meteorol. Soc.*, **114**, 399–420.
- Massman, W. (1997), An analytical one-dimensional model of momentum transfer by vegetation of arbitrary structure, *Bound.-Layer Meteorol.*, **83**, 407–421.
- McNaughton, K. G., and T. W. Spriggs (1986), A mixed-layer model for regional evaporation, *Boundary-Layer Meteorol.*, **74**, 262–288.
- Mecikalski, J. M., G. R. Diak, M. C. Anderson, and J. M. Norman (1999), Estimating fluxes on continental scales using remotely-sensed data in an atmosphere-land exchange model, *J. Applied Meteorol.*, **38**, 1352–1369.
- Menzel, W. P., W. L. Smith, and T. R. Stewart (1983), Improved cloud motion wind vector and altitude assignment using VAS, *J. Climate Appl. Meteorol.*, **22**, 377–384.
- Miller, D. A., and R. A. White (1998), *A conterminous United States multi-layer soil characteristics dataset for regional climate and hydrology modeling*, 42 pp, Earth Interactions.
- Myneni, R. B., et al. (2002), Global products of vegetation leaf area and fraction absorbed PAR from year one of MODIS data, *Remote Sens. Environ.*, **83**, 214–231.
- Norman, J. M., J.-L. Chen, and N. S. Goel (1990), Thermal emissivity and infrared temperature dependence of plant canopy architecture and view angle, paper presented at Proc. Tenth Annual Int. Geoscience Remote Sensing Symp. IEEE, Piscataway, N. J.
- Norman, J. M., W. P. Kustas, and K. S. Humes (1995), A two-source approach for estimating soil and vegetation energy fluxes from observations of directional radiometric surface temperature, *Agric. For. Meteorol.*, **77**, 263–293.
- Norman, J. M., M. C. Anderson, W. P. Kustas, A. N. French, J. R. Mecikalski, R. D. Torn, G. R. Diak, T. J. Schmugge, and B. C. W. Tanner (2003), Remote sensing of surface energy fluxes at 10¹-m pixel resolutions, *Water Resour. Res.*, **39**(8), 1221, doi:10.1029/2002WR001775.
- Otkin, J. A., M. C. Anderson, J. R. Mecikalski, and G. R. Diak (2005), Validation of GOES-based insolation estimates using data from the United States Climate Reference Network, *J. Hydromet.*, **6**, 460–475.
- Porté-Agel, F., M. B. Parlange, A. T. Cahill, and A. Gruber (2000), Mixture of time scales in evaporation: Desorption and self-similarity of energy fluxes, *Agron. J.*, **92**, 832–836.
- Priestley, C. H. B., and R. J. Taylor (1972), On the assessment of surface heat flux and evaporation using large-scale parameters, *Mon. Weather Rev.*, **100**, 81–92.
- Prueger, J. H., J. L. Hatfield, W. P. Kustas, L. E. Hipps, J. I. MacPherson, and T. B. Parkin (2005), Tower and aircraft eddy covariance measurements of water vapor, energy and carbon dioxide fluxes during SMA-CEX, *J. Hydrometeorol.*
- Ritchie, J. T. (1972), Model for predicting evaporation from a row crop with incomplete cover, *Water Resour. Res.*, **8**, 1204–1213.
- Schaafe, J. C., et al. (2004), An intercomparison of soil moisture fields in the North American Land Data Assimilation System (NLDAS), *J. Geophys. Res.*, **109**, D01590, doi:10.1029/2002JD003309.
- Schreiner, A. T., T. J. Schmit, and W. P. Menzel (2001), Observed trends of clouds based on GOES sounder data, *J. Geophys. Res.*, **106**(D17), 20,349–20,363.
- Shuttleworth, W. J., R. J. Gurney, A. Y. Hsu, and J. P. Ormsby (1989), FIFE, the variation on energy partition at surface flux sites, paper presented at Proc. IAHS Third Int. Assembly, IAHS, Washington, D. C.
- Song, J., M. L. Wesely, R. L. Coulter, and E. A. Brandes (2000), Estimating watershed evapotranspiration with PASS. Part I: Inferring root-zone moisture conditions using satellite data, *J. Hydrometeorology*, **1**, 447–461.
- Stewart, J. B., and S. B. Verma (1992), Comparison of surface fluxes and conductances at two contrasting sites within the FIFE area, *J. Geophys. Res.*, **97**, 18,623–18,628.
- Su, Z. (2002), The surface energy balance system (SEBS) for estimation of the turbulent heat fluxes, *Hydrology and Earth Sciences*, **6**, 85–99.
- Sugita, M., and W. Brutsaert (1991), Daily evaporation over a region from lower boundary layer profiles measured with radiosondes, *Water Resour. Res.*, **27**, 747–752.
- Tanner, C. B., and W. A. Jury (1976), Estimating evaporation and transpiration from a row crop during incomplete cover, *Agron. J.*, **68**, 239–242.
- Tanner, C. B., and T. R. Sinclair (1983), Efficient water use in crop production: research or re-search, in *Limits to efficient water use in crop production*, edited by H. M. Taylor et al., pp. 1–27, Am. Soc. Agron., Madison, WI.
- Twine, T. E., W. P. Kustas, J. M. Norman, D. R. Cook, P. R. Houser, T. P. Meyers, J. H. Prueger, P. J. Starks, and M. L. Wesely (2000), Correcting eddy-covariance flux underestimates over a grassland, *Agric. For. Meteorol.*, **103**, 279–300.
- Walthall, C., W. Dulaney, M. C. Anderson, J. M. Norman, H. Fang, and S. Liang (2004), A comparison of empirical and neural network approaches for estimating corn and soybean leaf area index from Landsat ETM+ imagery, *Remote Sens. Environ.*, **92**, 465–474.
- Wang, Y., et al. (2004), Evaluation of the MODIS LAI algorithm at a coniferous forest site in Finland, *Remote Sens. Environ.*, **91**, 114–127.
- Wood, E. F., D. P. Lettenmaier, and V. G. Zartarian (1992), A land-surface hydrology parameterization with subgrid variability for general circulation models, *J. Geophys. Res.*, **97**(D3), 2717–2728.
- Wu, X., G. R. Diak, C. M. Hayden, and J. A. Young (1995), Short-range precipitation forecasts using assimilation of simulated satellite water vapor profiles and cloud liquid water, *Mon. Wea. Rev.*, **123**, 347–365.
- Yang, W., et al. (2005), Validation of collections 3 and 4 Terra MODIS leaf area index and fraction vegetation absorbed photosynthetically active radiation products, *Remote Sens. Environ.*
- Zhang, L., and R. Lemeur (1995), Evaluation of daily evapotranspiration estimates from instantaneous measurements, *Agric. For. Meteorol.*, **74**, 139–154.

M. C. Anderson and W. P. Kustas, USDA-ARS Hydrology and Remote Sensing Laboratory, Bldg 007 Rm 104 BARC-West, Baltimore Ave, Beltsville, MD 20705, USA. (manderson@hydrolab.arsusda.gov)

J. R. Mecikalski, National Space Science and Technology Center, University of Alabama, Huntsville, AL, USA.

J. M. Norman, Department of Soil Science, University of Wisconsin, Madison, WI, USA.

J. A. Otkin, Cooperative Institute for Meteorological Satellite Studies, University of Wisconsin, Madison, WI, USA.